Korean J. Chem. Eng., 36(1), 136-145 (2019)
DOI: 10.1007/s11814-018-0157-y

pISSN: 0256-1115
eISSN: 1975-7220

Effects of electrode compression on the water droplet removal from proton exchange membrane fuel cells

Gholam Reza Molaeimanesh*,†, Mohammad Hassan Shojaeefard, and Mohammad Reza Moqaddari*****

*Research Laboratory of Automotive Fluids and Structures Analysis, School of Automotive Engineering, Iran University of Science and Technology, Tehran 16846-13144, Iran
**School of Mechanical Engineering, Iran University of Science and Technology, Tehran, Iran
***School of Automotive Engineering, Iran University of Science and Technology, Tehran, Iran
(*Received 30 May 2018 • accepted 27 September 2018*)

Abstract−Proton-exchange membrane (PEM) fuel cells are one of the main candidates for propulsion systems of modern electric vehicles. However, appropriate water management is crucial to performance. Cell compression can affect the performance and water management of PEM fuel cells. Although the influence of cell compression on the transport of continuous water flow through the porous electrodes has been investigated, the influence of cell compression on the droplet dynamic behavior through these electrodes is not investigated thoroughly. Employing a pore-scale simulation method such as lattice Boltzmann method (LBM) is an excellent means for such investigation. In this study, LBM was applied to investigate the influence of compression of gas diffusion layer (GDL) on the removal of a water droplet from an electrode of a cell with interdigitated flow field. During removal process the droplet dynamic movement through five different GDLs (one without compression and the other four with four different levels of compression) was depicted and analyzed. The results reveal that the droplet experiences a faster removal process when the GDL is compressed. However, more increasing of compression does not result in a faster removal process, which indicates the existence of an optimum compression level for which the fastest removal process occurs.

Keywords: Compression, Multiphase Flow, Water Droplet, Proton-exchange Membrane (PEM) Fuel Cell, Gas Diffusion Layer (GDL), Lattice Boltzmann Method (LBM)

INTRODUCTION

Proton exchange membrane (PEM) fuel cells have several advantages in comparison with conventional power sources such as high efficiency, ease of scalability and zero emission [1-3]. While many automotive manufacturers such as Mercedes-Benz and Nissan have decided to sell fuel cell electric vehicles (FCEVs) in the near future, Hyundai, Toyota and Honda currently sell FCEVs named Hyundai ix35, Toyota Mirai and Honda Clarity [4].

A stack of PEM fuel cells in an FCEV comprises several cells connected in series, while each cell consists of two electrodes and a membrane [5,6]. Stacking of cells is accompanied by compression and deformation of electrodes, especially at the most porous part of an electrode, which is the gas diffusion layer (GDL) [7-10]. Carbon papers which are usually used as GDLs in PEM fuel cells have fibrous microstructure [11] with a small Young's modulus [12]. Therefore, compression of carbon paper GDLs causes a considerable changes of their microstructure which can greatly affect the mass transport properties of them [13]. In fact, the main function of a GDL is to transfer reactants from channels toward catalyst layer for implementation of electrochemical reaction which may be affected by GDL compression and deformation.

The operation of PEM fuel cells usually suffers from accumulation of liquid water in the GDL (conventionally known as GDL flooding) which hinder the transferring of reactants toward catalyst layer [14,15]. In this regard, conducting simulations for analyzing the role of effective parameters on the water removal from GDL will be essentially beneficent for mitigating of GDL flooding [16]. Several studies have been conducted to investigate the water removal from various homogeneously and non-homogeneously compressed GDLs [13,17-21]. However, to the best of the authors' knowledge, in all of these studies the influence of GDL compression on the water removal is investigated, while the water is considered as a continuous liquid flow. Nevertheless, continuous flow of liquid water through the porous structure of a GDL in a PEM fuel cell is never in-situ observed and reported and conversely, some discrete small water droplets located among the fibrous structure of GDL are usually observed via the environmental scanning electron microscope [22,23]. In the current study, by inspecting dynamic behavior of a water droplet via pore-scale lattice Boltzmann (LB) simulation, the influence of GDL compression on droplet removal from the gas diffusion layer of a PEM fuel cell having interdigitated flow field is examined.

Lattice-Boltzmann method (LBM), which is a powerful numerical method for pore-scale simulation of multiphase flow through porous media, proposes valuable advantages such as ease of simulating fluid flow through complex structures, ease of parallelizing solution algorithm, etc. [24,25]. LBM, which is executed by solving simplified Boltzmann equation in a lattice, is widely used for elucidating dynamic behavior of a droplet through the gas diffusion layer

†To whom correspondence should be addressed.
E-mail: molaeimanesh@iust.ac.ir

of a PEM fuel cell [26-33].

NUMERICAL METHOD

1. LBM Framework

LBM is implemented via two main procedures: collision of particles and streaming of particles. Besides, these two procedures are performed in a lattice. In the present numerical investigation, in the collision procedure single relaxation time (SRT) operator (the well-known BGK operator [34]) is applied for modeling of particles collision and D2Q9 and D3Q19 lattice schemes are applied for 2D and 3D simulations. Furthermore, in order to model multi-phase flow, the pseudo-potential Shan and Chen (SC) model [35] is employed. Amid the proposed multi-phase LB models such as color model [36], pseudo-potential model [35] and free energy model [37], the effortless implementation and high adaptability of pseudo-potential SC model have made it an extensively attractive model for numerical specialists. In this model, a set of coupled LB equations with the following form [38],

$$f_i^k(\vec{r}+\vec{c}_i\Delta t,\ t+\Delta t)=f_i^k(\vec{r},\ t)+\frac{\Delta t}{\tau^k}[f_i^{k,\,eq}(\vec{r},\ t)-f_i^k(\vec{r},\ t)],\quad k=1,\ N \tag{1}$$

is solved. In the above equations, f_i^k denotes the density distribution function (DDF) of kth component (species) in the ith direction of lattice, $f_i^{k,eq}$ refers to the equilibrium value of f_i^k, $\vec{r}$ is the position vector in 2D or 3D space, t is time, $\vec{c}_i$ denotes the vector of velocity in the ith direction, τ^k is relaxation time of kth component, and N is the number of components. Equilibrium DDF is defined as:

$$f_i^{k,\,eq}=w_i\rho^k\left[1+\frac{\vec{c}_i\cdot\vec{u}^{k,\,eq}}{c_s^2}+\frac{1}{2}\frac{(\vec{c}_i\cdot\vec{u}^{k,\,eq})^2}{c_s^4}-\frac{1}{2}\frac{\vec{u}^{k,\,eq}\cdot\vec{u}^{k,\,eq}}{c_s^2}\right] \tag{2}$$

where w_i denotes the weighting factor of ith direction, $\rho^k=\sum_i f_i^k$ indicates the density of kth component, c_s denotes the sound speed in the lattice and $\vec{u}^{k,\,eq}$ refers to the equilibrium velocity of kth component. $\vec{u}^{k,\,eq}$ is defined as:

$$\vec{u}^{k,\,eq}=\frac{\sum_k\frac{1}{\tau^k}\sum_i f_i^k\vec{c}_i}{\sum_k\frac{1}{\tau^k}\rho^k}+\frac{\tau^k(\vec{F}_{coh}^k+\vec{F}_{adh}^k)}{\rho^k} \tag{3}$$

In the above definition, $\vec{F}_{coh}^k$ and $\vec{F}_{adh}^k$ refer to the forces acted on the kth component due to the interaction with the fluid and solid particles at the neighboring nodes, respectively. These forces are determined by [39]:

$$\vec{F}_{coh}^k(\vec{r},\ t)=-\psi^k(\vec{r},\ t)\sum_{j=1}^{N}G_{coh}^{kj}\sum_{i=0}^{M}w_i\psi^j(\vec{r}+\vec{c}\Delta t,\ t)\vec{c}_i \tag{4}$$

$$\vec{F}_{adh}^k(\vec{r},\ t)=-\psi^k(\vec{r},\ t)G_{adh}^k\sum_{i=0}^{M}w_i s(\vec{r}+\vec{c}\Delta t,\ t)\vec{c}_i \tag{5}$$

where ψ^k is a potential function for considering interaction of particles, G_{coh}^{jk} is the parameter tuning the cohesion between kth and jth components, G_{adh}^k is the parameter tuning the adhesion of kth component to a solid wall, and s is the solid function (a binary value function with 0 for fluid nodes of lattice and 1 for solid nodes of lattice). To perform successful LB simulations, the values of G_{coh}^{jk} s must be selected properly. Mostly the value of G_{coh}^{jk} is considered positive for k≠j and negative for k=j. Presented in Table 1 are the values of G_{coh}^{jk} s adopted in this study. Value of G_{adh}^k determines the wettability of the solid surface by kth component.

Table 1. Values of G_{coh}^{jk} adopted for 2D and 3D droplet tests in this study (1: water, 2: air)

G_{coh}^{11}	G_{coh}^{12}	G_{coh}^{21}	G_{coh}^{22}
−1.85	1.27	1.27	0.0

Several proposed relations can be found for ψ^k in the literature [35,39,40]. The original proposed relation by Shan and Chen [35] is employed in this study which states:

$$\psi^k=\rho_0^k\left(1-\exp\left(-\frac{\rho^k}{\rho_0^k}\right)\right) \tag{6}$$

where ρ_0^k is the reference density of kth component and it is set equal to 2 in the current i for all components.

Once $f_i^{k,eq}$ is calculated by Eq. (2), Eq. (1) is solved by implementing collision and streaming procedures shown in Eq. (7) and Eq. (8), respectively:

$$f_i^k(\vec{r},\ t+\Delta t)=f_i^k(\vec{r},\ t)\left[1-\frac{\Delta t}{\tau^k}\right]+\frac{\Delta t}{\tau^k}f_i^{k,\,eq}(\vec{r},\ t) \tag{7}$$

$$f_i^k(\vec{r}+\vec{c}_i,\ t+\Delta t)=f_i^k(\vec{r},\ t+\Delta t) \tag{8}$$

To perform collision and streaming procedures at the boundary nodes of computational lattice, DDFs which are aligned toward the interior of lattice must be known concerning the boundary condition type. For the boundary condition type of no-slip wall, bounce-back technique is often used for determining required DDFs. Bounce-back technique is a simple and powerful LB technique originally developed from the idea that if a particle hits a solid wall in a direction, it will be bounced back in the opposite direction. It incredibly empowers LBM for handling complicated geometries such as the pore structure of a porous medium with a simple structured lattice (i.e., complicated unstructured mesh is not required). Several forms of bounce-back technique have been presented [39]. In the current research, the famous mid-way form is used [39]. After calculating DDFs at every nodes of lattice in a time step, the following relations are applied for calculating the macroscopic velocity and pressure:

$$\vec{U}=\frac{\sum_{k=1}^{N}\sum_{i=0}^{18}f_i^k\vec{c}_i}{\sum_{k=1}^{N}\sum_{i=0}^{18}f_i^k}+\frac{1}{2}\frac{\sum_{k=1}^{N}\tau^k(\vec{F}_{coh}^k+\vec{F}_{adh}^k)}{\sum_{k=1}^{N}\sum_{i=0}^{18}f_i^k} \tag{9}$$

$$P=\frac{1}{3}\sum_{k=1}^{N}\sum_{i=0}^{18}f_i^k+\frac{1}{6}\sum_{k=1}^{N}G_{coh}^{kk}\psi^k\psi^k+\frac{1}{3}\sum_{k=1}^{N}G_{coh}^{jk}\sum_{j\neq k}\psi^k\psi^j \tag{10}$$

The overall implementation procedure of LBM is presented in Fig. 1.

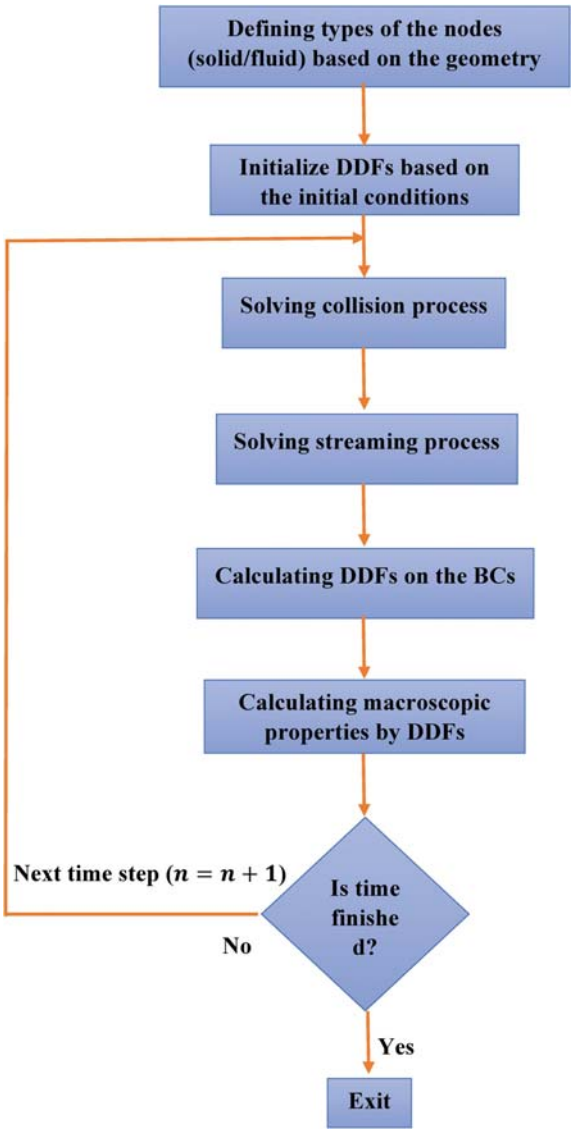

Fig. 1. Flowchart of LBM implementation procedure.

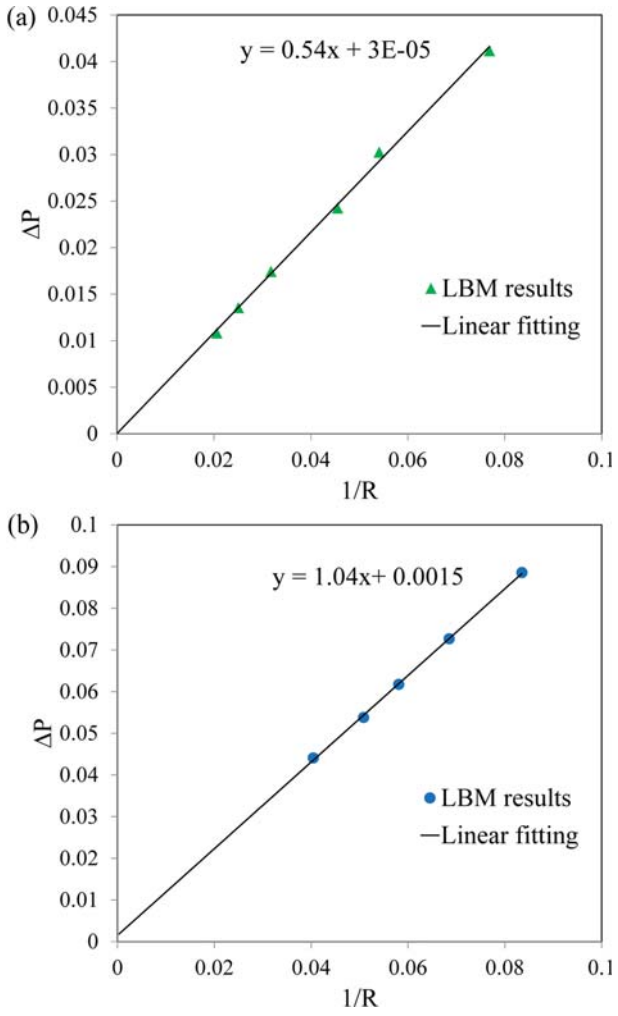

Fig. 2. Agreement of LBM results with Laplace law (linear relation of ΔP with 1/R): (a) 2D validation, (b) 3D validation.

2. Validation and Calibration of the Model

2-1. Validation Via Droplet Test

Well known Laplace law is used for validation of the numerical LB method. The law expresses the difference between the inside pressure and the outside pressure of a droplet is inversely proportional to the radius of droplet and proportional to the interfacial tension (σ):

$$\Delta p = \frac{p\sigma}{R} \tag{11}$$

where p=1 for a 2D droplet and p=2 for a 3D droplet. To perform validation via Laplace law a test known as droplet test is implemented by placing various droplets with various initial radiuses in the middle of a lattice. For all lateral boundaries, periodic boundary condition is used. In the current investigation, for validation of 2D and 3D simulations both 2D and 3D droplet tests were performed. In both tests, the initial densities of air and water inside the droplet were set to 0.025 and 5.25, respectively, while the initial densities of air and water outside the droplet were set to 2.0 and 0.0, respectively. The selected values for G_{coh}^{jk} factors for both 2D and 3D droplet tests are presented in Table 1. The pressure difference and the droplet radius are calculated till the steady state condition is achieved. The results are illustrated in Fig. 2 for both tests. As it is evidently depicted in this figure, the LBM results are in satisfactory agreement with the Laplace law for both 2D and 3D validation. The slope of fitted lines in Fig. 2 can be used for determining the interfacial tension in LB units. The results reveal that σ= 0.54 lm ts^{-2} for the 2D droplets and σ=0.52 lm ts^{-2} for the 3D droplets.

2-2. Calibration Via Static Contact Angle Test

The wettability of a surface is conventionally represented by its contact angle. More specifically, if the surface contact angle is smaller than 90^{o} it is known as a wetting or hydrophilic surface on which the liquid fluid tends to spread as a wetting layer. Conversely, if the surface contact angle is larger than 90^{o} it is known as a non-wetting or hydrophobic surface on which the liquid phase tends to shrink and appears as discrete droplets on the surface.

In the pseudo-potential SC LB model contact angle is governed

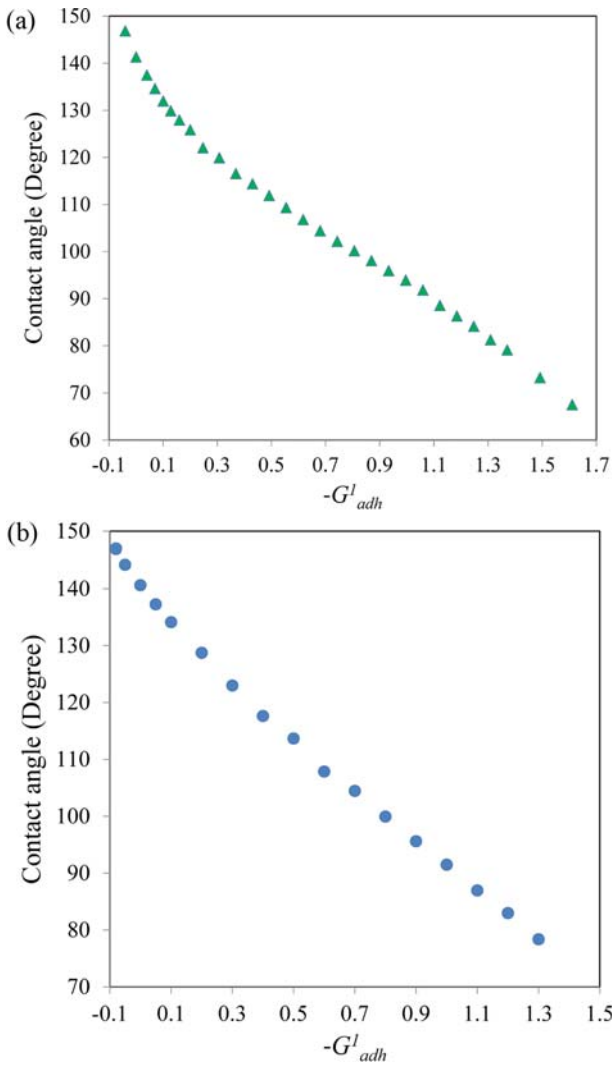

Fig. 3. The results of wettability calibration: (a) 2D calibration, (b) 3D calibration.

by G^{k}_{adh} factors, as stated before. The static contact angle test is implemented for determining the relation of G^{k}_{adh} factors and the contact angles; i.e., the static contact angle test is implemented to calibrate the wettability of the model. Noting that basically G^{1}_{adh} and G^{2}_{adh} can be changed independently, the relation $G^{1}_{adh}=-G^{2}_{adh}$ has been adopted in the current investigation. To calibrate the wettability, several 2D and 3D simulations with various G^{1}_{adh} factors were conducted and the results are presented in Fig. 3. For a particular simulation with a specific G^{1}_{adh} factor two semicircular (for 2D calibration) or semispherical (for 3D calibration) static droplets initially are placed on the bottom and top horizontal solid walls of the computational domain. Periodic boundary conditions are employed for all lateral surfaces. After steady state condition achieved the radius of droplet is calculated by:

$$R=\frac{(L/2)^2+H^2}{2H} \tag{12}$$

where H is the height of droplet and L is the length (for 2D droplets) or the diameter (for 3D droplets) of its contact region with the solid wall. After the droplet radius is determined, contact angle (θ) can be calculated by:

$$\theta=\begin{cases} 180^{o}-\tan^{-1}\left(\frac{L/2}{H-R}\right), & H>R \\ \tan^{-1}\left(\frac{L/2}{R-H}\right), & H\le R \end{cases} \tag{13}$$

MICROSTRUCTURE RECONSTRUCTION OF GDL

1. Generation of 3D GDL

To obtain the pore geometry of GDL (i.e., microstructure reconstruction of GDL) there are two general ways: combination of 2D sequential images and stochastic generation. Stochastic generation is a more convenient choice due to the low cost and ease of implementation [41]. In most LB simulations the stochastic reconstruction is used for microstructure reconstruction of GDL [11]. To reconstruct the fibrous structure of carbon paper GDL, the stochastic generation method proposed by Schladitz et al. [42] was applied in the current investigation. This method has also been applied in several other LB simulations [11]. In this method, the carbon fibers are stochastically generated and sequentially placed in the computational domain until the prescribed porosity is achieved. To stochastically generate carbon fibers, the following three assumptions are used:

(a) Fibers are considered as thin cylinders with uniform radius.
(b) Fibers have infinite length without any curvature.
(c) Overlapping of fibers is allowed.

The stochastic generation of fibers proceeds by stochastic generation of sequential lines. To specify the directional distribution of generated lines, a directional density function (p) is used. For conventional carbon papers this function is defined as:

$$p(\varphi,\theta)=\frac{1}{4\pi}\frac{\beta\sin\varphi}{(1+(\beta^2-1)\cos^2\varphi)^{3/2}},\quad \varphi\in[0,\pi),\ \theta\in[0,2\pi) \tag{14}$$

Due to the isotropy of conventional carbon papers in the material plane, this directional density function is independent of longitude (θ) for conventional carbon papers. Parameter β in the above equation is the anisotropy parameter which is used for anisotropy calibration in the direction normal to the material plane. After generation of a line, the nodes of the lattice whose vertical distances from the line are closer than the fiber radius are recognized as solid nodes. This procedure is repeated till the required porosity is attained.

The resulting stochastically generated microstructure is isotropic in the x-y plane and anisotropic in the z direction (the direction which is normal to the material plane). The degree of this anisotropy is characterized by anisotropy parameter, β, which is $0<\beta<\infty$ [42]. For $0<\beta<1$ carbon fibers have a higher probability for orienting normal to the x-y plane, whereas for $\beta>1$ carbon fibers have a higher probability for orienting parallel to the x-y plane. For the special case of $\beta=1$ carbon fibers distribute absolutely isotropically. In practical GDLs, β is has a large value, which denotes that carbon fibers are mostly oriented parallel to the x-y plane. Schulz et al. [41] analyzed SGL 10BA carbon paper and expressed its anisotropy parameter, fiber diameter and porosity values equal

100, 7 μm and 88%, respectively. In this investigation, the presented values by Schulz et al. [41] have been used for stochastic reconstruction of carbon paper GDL microstructure.

2. Attaining 2D GDL from the Generated 3D GDL

Since the computational cost for 3D pore-scale LB simulation of water droplet dynamic behavior through the GDL of a practical electrode is extensively high, 2D pore-scale simulations were conducted to investigate the role of GDL compression on the water droplet dynamic behavior. However, obtaining a realistic 2D microstructure of carbon paper is not a simple task. In the current investigation, a 3D 100×120×200 μm^3 GDL is generated at first (Fig. 4) and then the GDL in-plane permeability is calculated by LB simulation of the air flow through the GDL. After that, several in-plane sections of the 3D GDL are selected and their permeabilities are calculated via LB simulation of 2D air flow through them. The ratio between the permeabilities of 2D sections and the 3D GDL permeability is presented for 17 selected sections in Fig. 5. As this figure shows, the highest resemblance in terms of permeability exists for the section in y=104 μm. By repeating of this 100×200 μm^2 2D section, the 1,000×200 μm^2 2D GDL which is to be used for investigating the effect of GDL compression on the water droplet movement is generated.

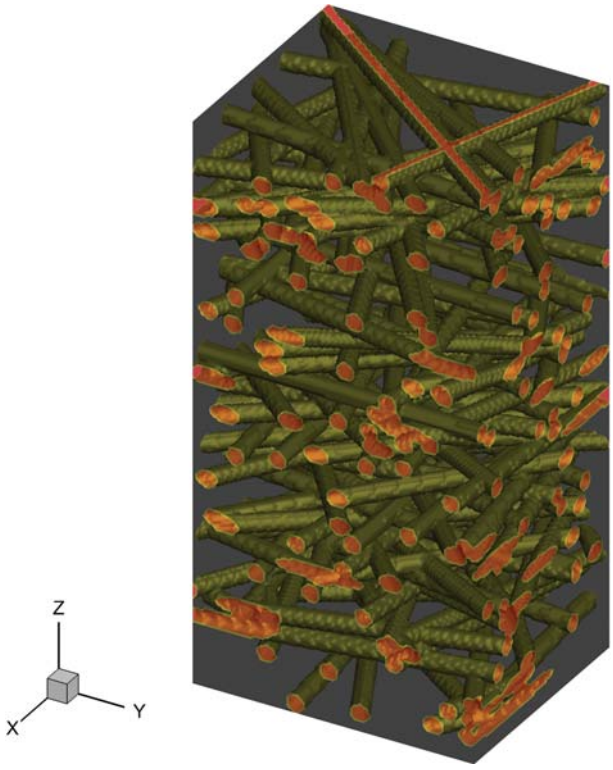

Fig. 4. The stochastically generated 3D GDL.

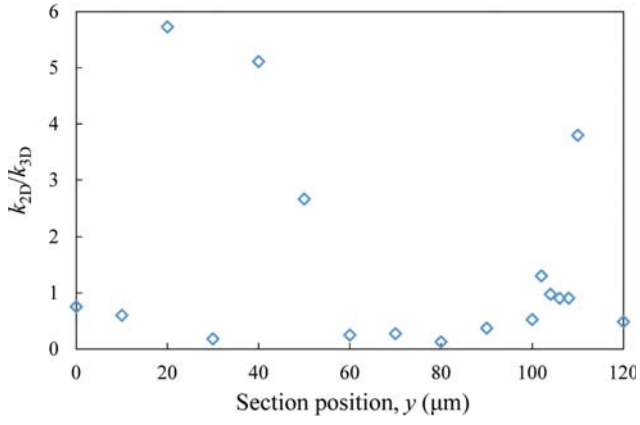

Fig. 5. The ratio between the permeabilities of 2D sections (k_{2D}) and the 3D GDL permeability (k_{3D}).

COMPUTATIONAL DOMAIN

The interdigitated flow field is designed to effectively remove water from GDL in PEM fuel cells. In this flow field, the air is distributed in a network of dead-end gas channels and consequently, it intrudes into the GDL material and passes the way under the lands until it reaches the network of outlet low-pressure gas channels (Fig. 6(a)). Shown in Fig. 6(b) is a section part of Fig. 6(a) which also represents the 2D computational domain in this study. It comprises the 2D GDL attained in the previous subsection at the bottom part accompanied by half of an inlet gas channel, land and half of an outlet gas channel at the top part. The horizontal line at the bottom of the computational domain indicates the interface of GDL and micro-porous layer (MPL). The blue circle with 50 μm

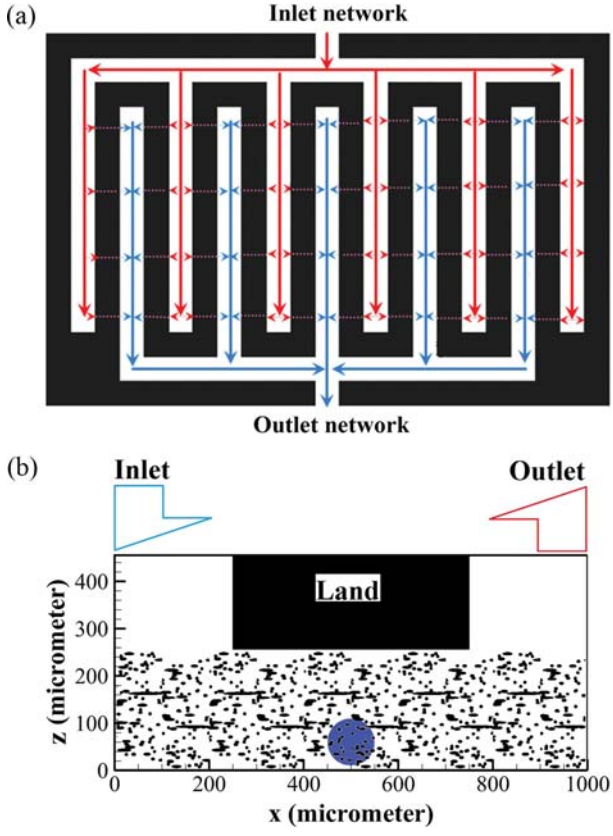

Fig. 6. A typical interdigitated flow field of a PEM fuel cell: (a) Top view, (b) a segment of side view which is also the computational domain.

radius represents the water droplet at the initial time.

Air is considered as an isothermal ideal gas. Dry air enters the computational domain with 0.1 m s^{-1} uniform velocity and exits the computational domain at 1.5 atm uniform pressure. To implement the mentioned boundary conditions at inlet and outlet, the Zou and He technique [43] is employed. Symmetry boundary condition is applied on the right and left vertical edges of the computational domain. No-slip boundary condition is employed on all solid walls. It is assumed that the contact angles of the MPL and the land are 150° and 85° [44], respectively, and the contact angle of carbon fibers equals 105°, same as the contact angle of polytetrafluoroethylene (PTFE); i.e., it is assumed that the carbon fibers are entirely treated by PTFE hydrophobic material. Once grid independency study is performed, a lattice with 1,000×455 grids is chosen in which the length of each lattice unit equals 1 μm.

In the current investigation, besides the uncompressed 2D GDL which is depicted in Fig. 6(b), the droplet dynamic behavior through four other compressed GDLs with four different levels of compression (first with 10% maximum relative deformation, second with 20% maximum relative deformation, third with 30% maximum relative deformation and the fourth with 40% maximum relative deformation) are also simulated. To attain the microstructure of the compressed GDL one must note that when the GDL is compressed by the lands of bipolar plates, the portions of GDL which are in direct contact with the lands experience the highest deformation. On the contrary, the portions of GDL which are more away from the lands experience less deformation. In the current study, it is assumed that the portion of 2D GDL shown in Fig. 6(b) which is in direct contact with the land (i.e., for 250 μm≤x≤750 μm) experiences the deformation entirely, while other parts of GDL (i.e., for 0 μm≤x<250 μm and 750 μm<x≤1,000 μm) experience the deformation partially. This partial deformation is assumed to have a linear distribution with minimum zero value at the two extremes of computational domain. More specifically, for the case with 10% maximum relative deformation the height of each solid node located on a carbon fiber after compression (z′) is related to its height before compression (z) via:

$$z' = \begin{cases} 0.9z\dfrac{x}{250}, & for\ 0 \le x < 250 \\ 0.9z, & for\ 250 \le x \le 750 \\ 0.9z\left(\dfrac{1{,}000 - x}{250}\right), & for\ 750 < x \le 1{,}000 \end{cases} \quad (15)$$

For the cases with 20%, 30% and 40% maximum relative deformation the pre-factor in the above equation must be changed from 0.9 to 0.8, 0.7 and 0.6, respectively.

RESULTS AND DISCUSSION

The dynamic behavior of a water droplet with 50 μm initial radius during removal from an uncompressed GDL is depicted in Fig. 7. As Figs. 7(a)-(e) show, the air stream entering the GDL from the inlet and traveling under the land toward the outlet causes the droplet to move between hydrophobic carbon fibers toward the outlet.

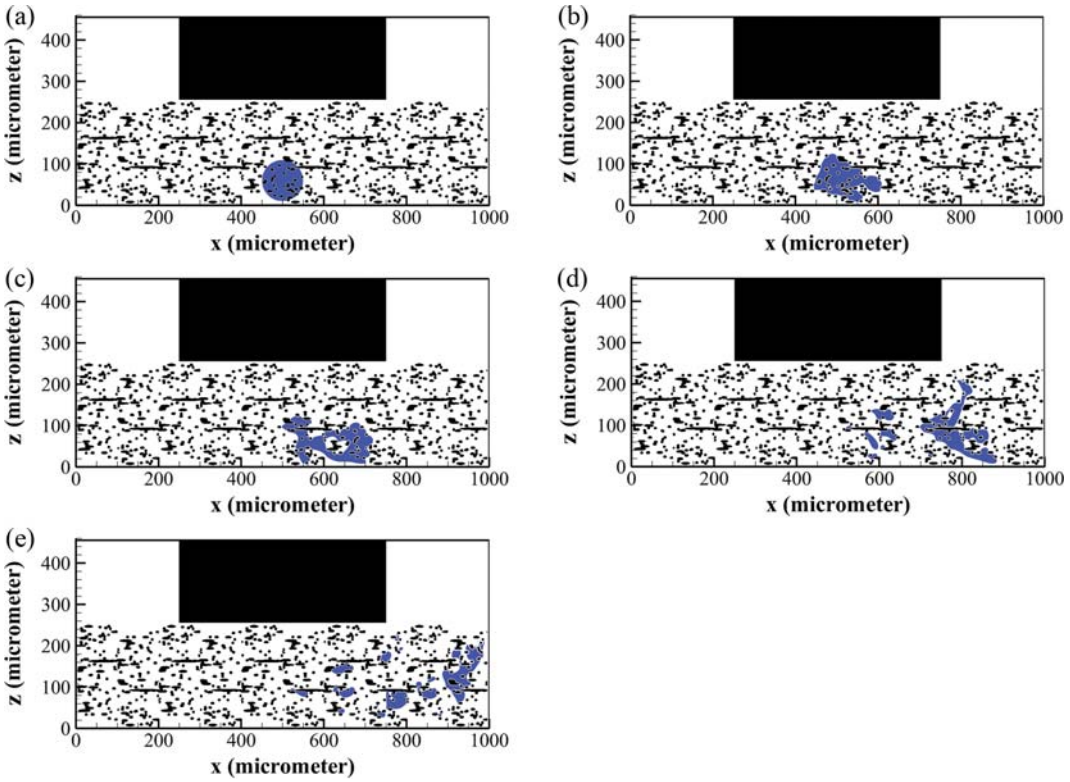

Fig. 7. Removal process of water droplet from the uncompressed GDL: (a) 0 ts, (b) 10,000 ts, (c) 20,000 ts, (d) 30,000 ts, (e) 40,000 ts.

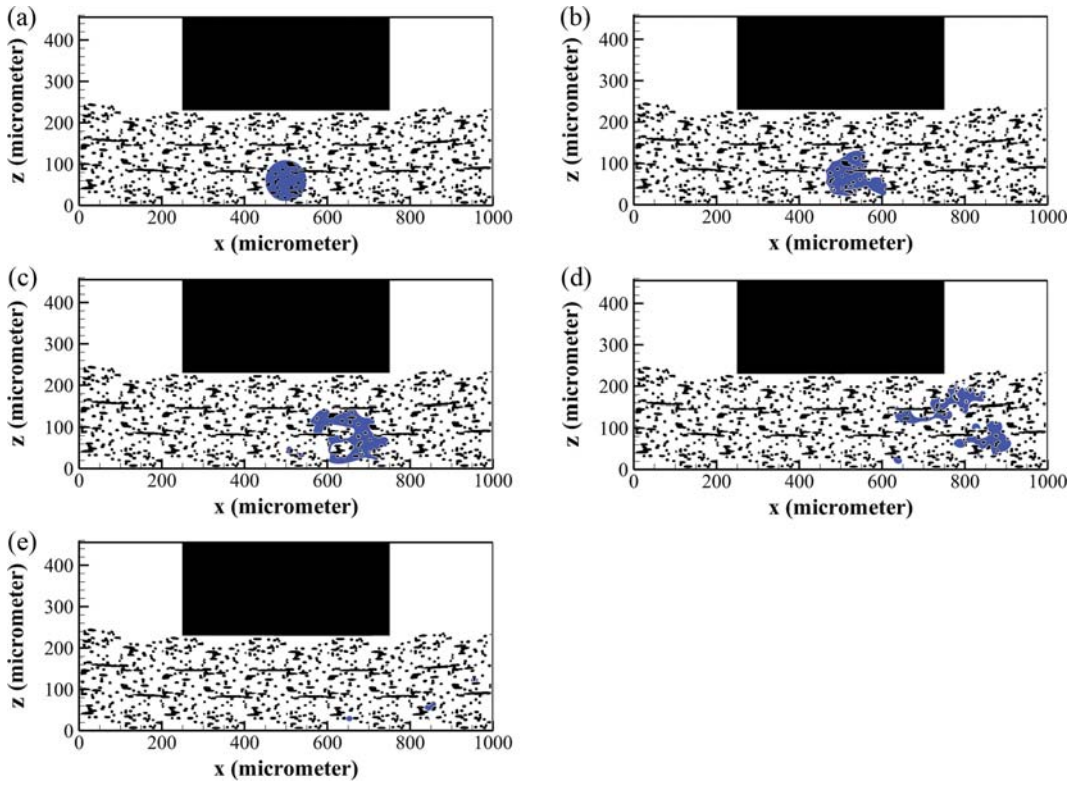

Fig. 8. Removal process of water droplet from the GDL with 10% maximum relative deformation: (a) 0 ts, (b) 10,000 ts, (c) 20,000 ts, (d) 30,000 ts, (e) 40,000 ts.

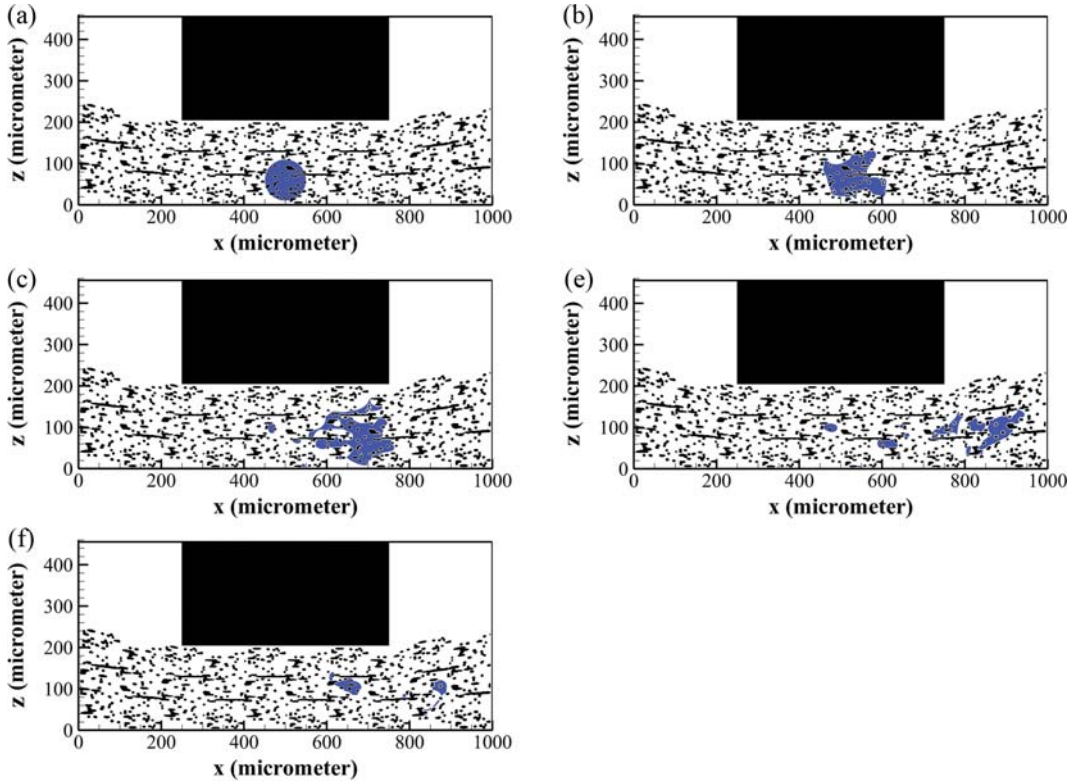

Fig. 9. Removal process of water droplet from the GDL with 20% maximum relative deformation: (a) 0 ts, (b) 10,000 ts, (c) 20,000 ts, (d) 30,000 ts, (e) 40,000 ts.

However, on the way toward the outlet, due to its relatively large size it is broken into a few parts by fronted fibers. The resulting smaller parts can move more easily among fibers; however, some of them may be trapped between fibers and can only be evaporated. Therefore, after about 40,000 time steps (each time step equals 7.94×10^{-9} s and hence, 40,000 time steps is approximately 0.32 ms) some water still remains in the domain.

Shown in Fig. 8 is the water droplet dynamic behavior through the GDL with 10% maximum relative deformation during the removal process. The land has come down 10% and it has compressed the GDL. Therefore, the distance between the land and MPL in this figure is less than the similar space in Fig. 7. Besides, the average pore size in this case is smaller than the average pore size in the uncompressed case. These facts indicate that the average velocity of air during its traveling under the land has increased, which can be regarded as a positive fact for inertial removal of water droplet. Therefore, after about 40 time steps no significant amount of water remains in the GDL.

Fig. 9 shows the dynamic behavior of droplet during ejection from the GDL with 20% maximum relative deformation. More coming down of land and more compression of GDL in this case leads to highest average velocity of air stream traveling under the land and hence, the fastest removal process may be expected. However, one must note that by reducing the average pore size the viscous force acting on the droplet by the surrounding fibers is also increased. This acts as a negative force against the removal of water droplets. Consequently, the question that whether compression assists or hinders the removal process of a water droplet from GDL may not have a unique answer.

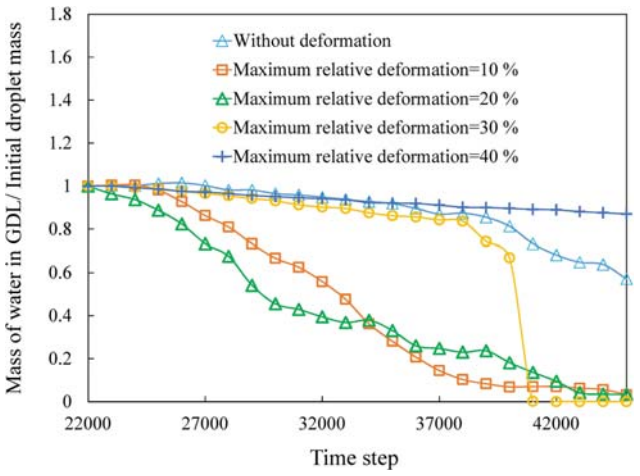

Fig. 10. The time evolution of normalized mass of water in the GDL.

The evolution of normalized mass of water (i.e., the ratio between mass of water in the GDL and the initial water droplet mass) versus time is presented in Fig. 10 for the five investigated GDLs. As the slope of the curves in this figure shows, the water droplet removal from the uncompressed GDL is significantly slower than the droplet removal from compressed GDLs with 10%, 20% and 30% maximum relative deformation; this represents the considerable influence of compression. In fact, in these three compressed GDLs the droplet is almost completely removed after 45,000 time

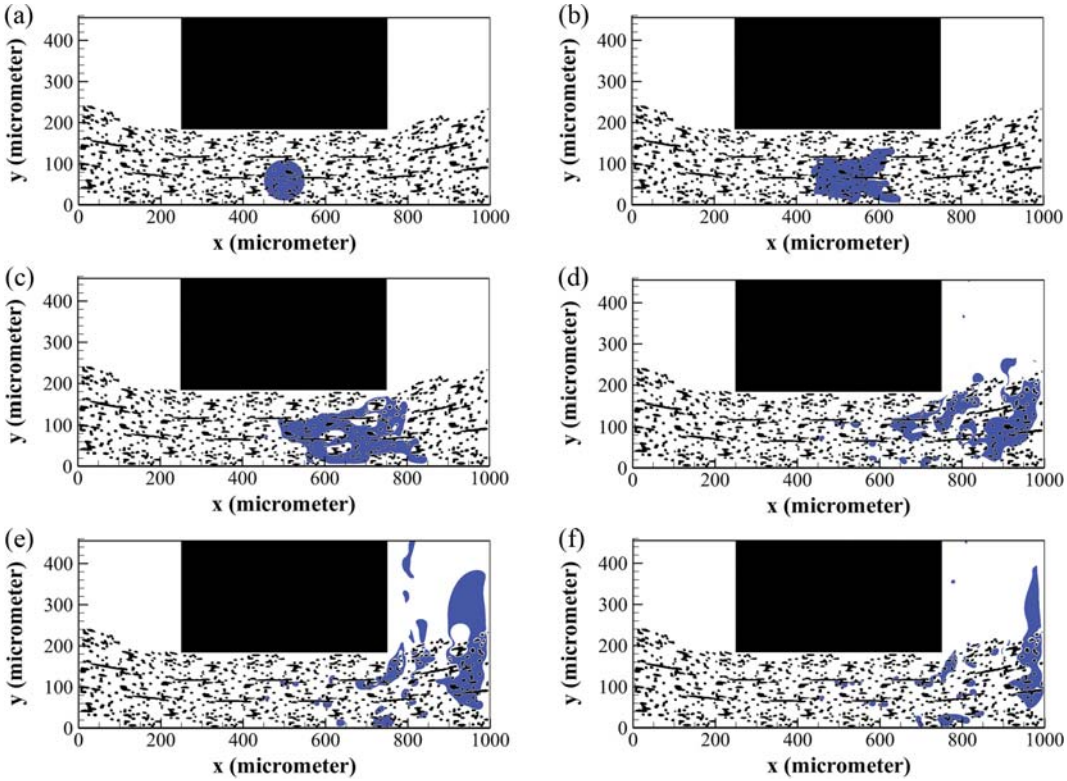

Fig. 11. Removal process of water droplet from the GDL with 30% maximum relative deformation: (a) 0 ts, (b) 10,000 ts, (c) 20,000 ts, (d) 30,000 ts, (e) 35,000 ts, (f) 38,000 ts.

steps, while in the uncompressed GDL more than half of droplet mass remains in the domain after such period of time. In fact, only a small portion of the initial droplet is ejected at about 40,000 time steps, which causes an increase in water removal rate at about 40,000 time steps for this case.

However, comparison of the four compressed GDLs is not so straightforward. In fact, in earlier times the GDL with 20% maximum relative deformation shows a better removal process, while in later times the GDL with 10% maximum relative deformation shows a better removal process. In fact, the changes of the slopes of the water removal rate along the time for the GDL with 20% maximum relative deformation is due to the fact that ejecting of small portions of the droplet from GDL is a discrete phenomenon (i.e., droplet portions are ejected one by one); and, by ejecting of each portion, the removal rate accelerates a bit.

For the maximum relative deformation of 30% the figure shows that in earlier times the slope of water removal is slow because the degree of compression is high and the pore spaces are downsized, which makes water movement difficult. However, finally the droplet can eject entirely (i.e., without breaking down to portions) from GDL at about 40,000 time step in this case, which is illustrated in Fig. 11; this is the cause of the sharp descent of the related curve. More increasing of compression to 40% makes the situation more severe, and water droplet removal from GDL cannot happen. As a whole, no significant improvement can be seen when the compression is increased from 30% to 40%. Therefore, increasing of compression does not necessarily lead to better water management. This is because by increasing of compression the inertial force of air in the pore space increases, while the viscous force acting on the water by the neighboring fibers is also increased. There is a trade-off between these two opposite forces, and hence there might be an optimum level of compression for which the best removal process can be observed. However, the amount of this optimum value can be affected by droplet size and fibers wettability, which can be the subject of future studies.

CONCLUSIONS

The effect of cell compression on the droplet dynamic behavior through five GDLs (one without compression and the other four with four different levels of compression) in a PEM fuel cell GDL with interdigitated flow filed design was investigated. To simulate droplet movement through GDL, the famous Shan and Chen multi-species multi-phase LB model is validated, calibrated and employed. The removal process of droplet from five different GDLs was presented and analyzed. Due to the relatively large size of initial droplet, it is broken into a few parts by fronted fibers on the way toward the outlet and the resulted smaller parts move more easily among the fibers.

By compressing the GDL, the distance between the land and MPL is reduced and hence, the average pore size will decrease, which consequently leads to higher air velocity through the pore space of GDL. Therefore, compressing the GDL enhances the droplet removal process. However, by more increasing of compression a faster removal process was not achieved. This is because applying compression on the GDL leads to more viscous (capillary) attraction by the neighboring fibers, and this negative fact can hinder the droplet removal process. In fact, there is a trade-off between these two opposite facts, and hence there might be an optimum level of compression for which the easiest removal process can be achieved. However, the amount of this optimum value can be influenced by the droplet size and the fibers wettability.

NOMENCLATURE

$\vec{c}_i$: velocity of particle in the ith direction of lattice [lu ts^{-1*}]
c_s : sound speed through the lattice [lu ts^{-1}]
$\vec{F}^k_{adh}$: force acting on a particle of kth species from neighboring solid nodes [lm lu ts$^{-2\dagger}$]
$\vec{F}^k_{coh}$: force acting on a particle of kth species from neighboring fluid nodes [lm lu ts^{-2}]
f^k_i : density distribution function of kth species in the ith direction of lattice
G^{kj}_{coh} : cohesion factor between kth and jth species
G^k_{adh} : adhesion factor of kth species to the solid wall
H : droplet height [lu]
L : contact region length [lu]
P : pressure of flow [lm lu^{-1} ts^{-2}]
R : radius of droplet [lu]
$\vec{r}$: position vector of particle [lu]
T : time [ts]
$\vec{U}$: velocity of flow [lu ts^{-1}]
$\vec{u}^{k,\,eq}$: equilbrium velocity of kth component [lu ts^{-1}]
w_i : weighting factor of ith direction
x, y, z : cartesian coordinates [mm]
z′ : height after compressing GDL [mm]

Greek Symbols

β : anisotropy parameter
θ : static contact angle; also longitude in spherical coordinates
ρ : density [lm lu^{-3}]
φ : lattitude in spherical coordinates
σ : interfacial tension
τ : relaxation time [ts]
ψ^k : potential function of kth species

Abbreviations

DDF : density distribution function
GDL : gas diffusion layer
LB : Lattice-Boltzmann
LBM : Lattice-Boltzmann method
MPL : microporous layer
PEM : proton-exchange membrane
PTFE : poly tetra fluoro ethylene
SC : Shan and Chen

REFERENCES

1. M. Ehsani, Y. Gao and A. Emadi, Modern electric, hybrid electric,

*ts and lu indicate LB units of time and length, respectively.
†lm indicates LB unit of mass.

and fuel cell vehicles: fundamentals, theory and design, CRC Press, London (2012).
2. K. Hongthong, K. Pruksathorn, P. Piumsomboon and P. Sripakagorn, *Korean J. Chem. Eng.*, **24**, 612 (2007).
3. T. Kim, H. Lee, W. Sim, J. Lee, S. Kim, T. Lim and K. Park, *Korean J. Chem. Eng.*, **26**, 1265 (2009).
4. Fuel cell vehicles, https://en.wikipedia.org/wiki/Fuel_cell, 2016 (accessed 3 January 2016).
5. D. J. Moon, J. W. Ryu, S. D. Lee and B. S. Ahn, *Korean J. Chem. Eng.*, **19**, 921 (2002).
6. B. Nakrumpai, K. Pruksathorn and P. Piumsomboon, *Korean J. Chem. Eng.*, **23**, 570 (2006).
7. W. Chen and F. Jiang, *Int. J. Hydrogen Energy*, **41**, 8550 (2016).
8. I. S. Han, S. K. Park and C. B. Chung, *Korean J. Chem. Eng.*, **33**, 3121 (2016).
9. S. Park and B. N. Popov, *Korean J. Chem. Eng.*, **31**, 1384 (2014).
10. S. Bhlapibul and K. Pruksathorn, *Korean J. Chem. Eng.*, **25**, 1226 (2008).
11. M. H. Shojaeefard, G. R. Molaeimanesh, M. Nazemian and M. R. Moqaddari, *Int. J. Hydrogen Energy*, **41**, 20276 (2016).
12. M. F. Serincan and U. Pasaogullari, *J. Power Sources*, **196**, 1314 (2011).
13. A. Mahmoudi, A. Ramiar and Q. Esmaili, *Energy Convers. Manag.*, **110**, 78 (2016).
14. K. Tüber, D. Pócza and C. Hebling, *J. Power Sources*, **124**, 403 (2003).
15. M. Mortazavi and K. Tajiri, *J. Power Sources*, **245**, 236 (2014).
16. C. S. Lee and S. C. Yi, *Korean J. Chem. Eng.*, **21**, 1153 (2004).
17. P. P. Mukherjee, C.-Y. Wang, V. P. Schulz, Q. Kang, J. Becker and A. Wiegmann, *ECS. Trans.*, **25**, 1485 (2009).
18. Z. Shi, X. Wang and L. Guessous, *J. Fuel Cell. Sci. Technol.*, **7**, 021012 (2010).
19. Y. Wang and K. S. Chen, *J. Electrochem. Soc.*, **158**, B1292 (2011).
20. P. Chippar, O. Kyeongmin, K. Kang and H. Ju, *Int. J. Hydrogen Energy*, **37**, 6326 (2012).
21. T. Tranter, A. Burns, D. Ingham and M. Pourkashanian, *Int. J. Hydrogen Energy*, **40**, 652 (2015).
22. J. H. Nam and M. Kaviany, *Int. J. Heat. Mass Transf.*, **46**, 4595 (2003).
23. F. Zhang, X. Yang and C. Wang, *J. Electrochem. Soc.*, **153**, A225 (2006).
24. S. Chen and G. D. Doolen, *Annu. Rev. Fluid Mech.*, **30**, 329 (1998).
25. G. R. Molaeimanesh and M. H. Akbari, *Korean J. Chem. Eng.*, **32**, 397 (2015).
26. G. R. Molaeimanesh, H. S. Googarchin and A. Q. Moqaddam, *Int. J. Hydrogen Energy*, **41**, 22221 (2016).
27. G. R. Molaeimanesh and M. H. Akbari, *Int. J. Hydrogen Energy*, **39**, 8401 (2014).
28. G. R. Molaeimanesh and M. H. Akbari, *Korean J. Chem. Eng.*, **31**, 598 (2014).
29. L. Chen, H.-B. Luan, Y.-L. He and W.-Q. Tao, *Int. J. Therm Sci.*, **51**, 132 (2012).
30. Y. B. Salah, Y. Tabe and T. Chikahisa, *Energy Procedia*, **28**, 125 (2012).
31. B. Han and H. Meng, *J. Power Sources*, **217**, 268 (2012).
32. B. Han, J. Yu and H. Meng, *J. Power Sources*, **202**, 175 (2012).
33. L. Hao and P. Cheng, *J. Power Sources*, **190**, 435 (2009).
34. P. L. Bhatnagar, E. P. Gross and M. Krook, *Phys Rev.*, **94**, 511 (1954).
35. X. Shan and H. Chen, *Phys Rev. E.*, **47**, 1815 (1993).
36. A. K. Gunstensen, D. H. Rothman, S. Zaleski and G. Zanetti, *Phys. Rev. A.*, **43**, 4320 (1991).
37. M. R. Swift, W. R. Osborn and J. M. Yeomans, *Phys. Rev. Lett.*, **75**, 830 (1995).
38. A. A. Mohamad, Lattice Boltzmann method: fundamentals and engineering applications with computer codes, Springer, New York (2011).
39. M. C. Sukop and D. T. Thorne, Lattice Boltzmann modeling, an introduction for geoscientists and engineers, Springer, Heidelberg (2007).
40. P. Yuan and L. Schaefer, *Phys. Fluids*, **18**, 042101 (2006).
41. V. P. Schulz, J. Becker, A. Wiegmann, P. P. Mukherjee and C.-Y. Wang, *J. Electrochem. Soc.*, **154**, B419 (2007).
42. K. Schladitz, S. Peters, D. Reinel-Bitzer, A. Wiegmann and J. Ohser, *Comput. Mater. Sci.*, **38**, 56 (2006).
43. Q. Zou and X. He, *Phys. Fluids*, **9**, 1591 (1997).
44. E. Kumbur, K. Sharp and M. Mench, *J. Power Sources*, **168**, 356 (2007).